Letter

# Elucidating the Photoresponse of Ultrathin MoS Field-Effect Transistors by Scanning Photocurrent Microscopy

Chung-Chiang Wu, Deep Jariwala, Vinod K. Sangwan, Tobin J. Marks, Mark C Hersam, and Lincoln J. Lauhon

*J. Phys. Chem. Lett.*, **Just Accepted Manuscript** • DOI: 10.1021/jz401199x • Publication Date (Web): 17 Jul 2013

# Elucidating the photoresponse of ultrathin $MoS_2$ field-effect transistors by scanning photocurrent microscopy

Chung-Chiang Wu[1||], Deep Jariwala[1||], Vinod K. Sangwan[1], Tobin J. Marks[1,2], Mark C. Hersam[1,2,3], and Lincoln J. Lauhon[1*]

[1]Department of Materials Science and Engineering, Northwestern University, Evanston, IL 60208, USA

[2]Department of Chemistry, Northwestern University, Evanston, IL 60208, USA

[3]Department of Medicine, Northwestern University, Evanston, IL 60208, USA

|| These authors contributed equally.

**Abstract:**

The mechanisms underlying the intrinsic photoresponse of few-layer (FL) molybdenum disulphide ($MoS_2$) field-effect transistors are investigated *via* scanning photocurrent microscopy. We attribute the locally enhanced photocurrent to band-bending assisted separation of photoexcited carriers at the $MoS_2$/Au interface. The wavelength-dependent photocurrents of few layer $MoS_2$ transistors qualitatively follow the optical absorption spectra of $MoS_2$, providing direct evidence of interband photoexcitation. Time and spectrally resolved photocurrent measurements at varying external electric fields and carrier concentrations establish that drift-diffusion currents dominate photothermoelectric currents in devices under bias.

TEXT:

The layered transition metal dichalcogenides (TMDCs)[1] have attracted great interest recently due to their intriguing electrical and optical properties.[2-8] Field-effect transistors (FETs) fabricated with single layer (SL) and few layer (FL) $MoS_2$ have shown both unipolar[9-11] and ambipolar[12] charge transport characteristics with high in-plane electron mobility concurrent with high on/off current ratios[9,13] and large current-carrying capacity[10]. While bulk $MoS_2$ is an n-type semiconductor with an indirect bandgap of ~1.3 eV[14], single-layer $MoS_2$ has a direct bandgap of ~1.8 eV[15,16], which leads to enhanced photoluminescence (PL) compared to bilayer and thicker samples. The combination of a large bandgap in the visible region, strong photoresponse, light emission, and high field-effect mobility makes $MoS_2$ a promising 2D semiconductor for a variety of electronic[6,17,18] and optoelectronic[7,19,20] applications. Besides the above mentioned, several other interesting properties such as piezoelectricity,[21] tunability of band gaps and phase transitions with electric field, strain and composition[22-25] have also been predicted for ultrathin TMDCs. Solution processed two dimensional materials, decorated with metal nanoparticles or quantum dots (QDs) have also been heavily investigated as catalysts and electrode materials in photochemical reactions.[26-28] The high surface area, coupled with a band gap in visible part of the electromagnetic spectrum, makes these ultrathin dichalcogenide based catalysts attractive candidates for solar water splitting.[29-32] The interface of these nanoparticles with $MoS_2$ plays a deterministic role in the charge transfer kinetics and efficiency of such photoelectrochemical reactions.[33,34] Thus, the behavior of photoexcited carriers in a controlled FET geometry is relevant to both optoelectronic and energy conversion applications.

The photoresponse of $MoS_2$-based optoelectronic devices has been attributed to various mechanisms including photoconductivity,[19] photovoltaic effects,[35] and the photothermoelectric

(PTE) effect.[36] More specifically, global illumination of $MoS_2$ FETs has produced photocurrents and open circuit voltages ascribed to photoconductivity changes[19] and photovoltaic effects,[35] respectively. In contrast, a recent study employing local illumination with a focused beam concluded that the PTE effect dominates the photoresponse of SL $MoS_2$ FETs with ohmic contacts.[36] Prior work on carbon nanotube and graphene devices has revealed a similar diversity of behaviors that can inform investigations of $MoS_2$. The PTE effect predominates in carbon nanotube FETs under some circumstances,[37-39] and the contributions of photovoltaic and thermoelectric signals in graphene have been convincingly isolated.[40-48] For example, the graphene photovoltaic response dominates the PTE response under applied bias and at continuous wave excitation at low temperatures.[40,47]

Here we employ a combination of spectroscopic and time-resolved scanning photocurrent microscopy (SPCM) measurements to identify the nature of the photoresponse of ultrathin $MoS_2$ FETs under a comprehensive range of source-drain and gate biasing conditions including depletion, accumulation, and saturation. Although we fabricated and measured devices consisting of SL, 3L and 4L $MoS_2$ flakes, we focus our analysis on 4L $MoS_2$ FETs because they can be biased into saturation in air without being damaged. We conclude that the photocurrent is dominated by drift and diffusion of photoexcited carriers in regions of high electric field, both in the device channel and adjacent to the $MoS_2$/Au contacts. The photocurrent absorption spectra in $MoS_2$ flakes of different thicknesses, the photoresponse time, and the bias dependencies of the photocurrent provide a comprehensive picture of the nature of the response.

FETs were fabricated by e-beam lithography on mechanically exfoliated $MoS_2$ flakes on $n^+$-Si/$SiO_2$ (300 nm) substrates.[11] $MoS_2$ flakes were first screened by optical contrast imaging, and the thickness of each flake was characterized by Raman spectroscopy[49] (see Supporting

Information S1). Raman spectra (Figure S1) obtained from three samples are assigned to single- (SL), triple- (3L) and quadruple- (4L) layer $MoS_2$, respectively. The peak at ~385 $cm^{-1}$ corresponds to the in plane ($E_{2g}^1$) mode, and the peak at ~404 $cm^{-1}$ is attributed to the out of plane ($A_{1g}$) mode.[49] The $E_{2g}^1$ mode softens and $A_{1g}$ mode stiffens with increasing number of layer. In this manner, the frequency difference between these two modes was employed to determine $MoS_2$ thickness.[49]

Figure 1a shows a schematic of the experimental setup and the geometry of a typical $MoS_2$ FET. A scanning confocal microscope (WiTec) coupled to a tunable coherent white light source (NKT Photonics) is used to generate the spatially- and spectrally-resolved photocurrent, which is converted into a voltage by a current preamplifier and recorded by either a lock-in amplifier (for imaging) or a digital sampling oscilloscope (for temporally resolved measurements). The reflected light is recorded simultaneously to correlate the spatial photocurrent map with the device geometry. A representative photocurrent image of a 4L device is shown in Figure 1b for zero drain-source bias, an excitation wavelength $\lambda$=550 nm, and an excitation power of 20 μW. Positive (bright) and negative (dark) photocurrent is observed near the edge of the source (S) and drain (D) contacts, respectively. Qualitatively similar behavior is also observed in the SL device (see Supporting Information S2). The transfer characteristic of the 4L $MoS_2$ FET (Figure 1c) exhibits n-type semiconducting behavior with a field-effect mobility of ~8 $cm^2/Vs$, a typical value for FL $MoS_2$ FETs on $SiO_2$ dielectrics when measured under ambient conditions without encapsulation.[50,51] The output plot of the 4L device is linear at a low drain bias (Inset in Figure 1c) in agreement with prior reports that Au forms an ohmic contact.[9,52] In addition, the output plot shows a saturation regime consistent with the formation of a pinch-off region as $V_{DS}$ exceeds $V_G$-$V_T$; direct evidence of pinch-off is provided below. The 4L output

plot is well described by the quadratic current versus voltage relationship expected for a conventional planar FET[6], giving $V_T$ = -9.3 V. We note that linear current versus voltage characteristics can be observed even in the presence of a Schottky barrier if charge injection is dominated by tunneling.[53] This may be the case in the devices under consideration, although we also note that the channel resistance likely dominates the contact resistance.[54] As discussed further below, some degree of band bending near the contacts can be expected considering the recent report of electroluminescence at the $MoS_2$-metal interface.[55] An analysis of carrier lifetime ($\tau$) and minority carrier diffusion length ($L_D$) enabled by the SPCM measurement is presented in Supporting Information section S3.

An important goal of the SPCM characterization is to identify the dominant photocurrent generation mechanisms in different transistor biasing regimes, as such understanding can aid in the interpretation and optimization of transistor performance[56] and inform the design of photodetectors. Towards that end, we establish that the dominant photocurrent under bias results from interband absorption within the $MoS_2$, rather than absorption in the metal contacts. The constant power (20 μW) photocurrent spectra in Figures 2a are consistent with interband absorption in $MoS_2$. Ultra-thin $MoS_2$ has two absorption peaks at ~600 nm and ~660 nm due to the spin-orbital splitting of the valence band (although the lower energy peak of a 4L device is not clearly resolved). We note that wavelength-dependent thin-film interference within the underlying dielectric also influences the absorption in the $MoS_2$, but to a smaller extent. Qualitatively, the semi-log plots of photocurrent vs. excitation wavelength of SL, 3L, and 4L $MoS_2$ FETs show the thickness dependent transition from indirect to direct interband photoexcitation (Figure 2b), but the onset of the indirect gap is not sufficiently resolved to justify fitting. In further analyses and discussion below, we can safely assume that observed

photocurrents originate from inter-band excitation in the $MoS_2$ rather than carrier generation in or heating of the metal contacts.

Studies of the local photocurrent in the 4L device under varying applied biases (Figure 3) were used to analyze FET performance and aide in the identification of the photocurrent generation mechanisms. As shown in the middle panel of Figure 3a, the Au contact induces upward band bending in the n-type semiconductor with an estimated Schottky barrier of ~400 meV based on the work function differences of Au and $MoS_2$ ($\Phi_{SB} = \Phi_{Au} - \Phi_{MoS_2}$).[55] Band bending induced photocurrent near contacts has been widely reported in devices based on silicon nanowires,[57,58] carbon nanotubes,[59,60] and graphene.[40,42,45,61] When $MoS_2$ is illuminated near the drain contact, the built-in electric field drives holes to the drain electrode while electrons move towards the source electrode, resulting in a negative photocurrent. The same process induces a positive photocurrent upon illumination near the source electrode. In addition, photothermoelectric (PTE) currents of the same sign are produced due to the heating of the junction produced by laser illumination.[36]

To explore the regime in which drift currents dominate PTE effects, photocurrent images were generated at moderate source-drain biases (Figure 3a). In the linear regime (0.5 V to –0.5 V, see Figure 1c inset), variations in $V_{DS}$ lead to enhancement and suppression of the photocurrent at opposite contacts, reflecting modulation of the near contact band bending (Figure 3a). A positive $V_{DS}$ increases the band bending at the source contact, resulting in an increase in the magnitude of the photocurrent, whereas the reduced band bending at the drain contact suppresses the photocurrent. The same behavior is observed when the bias is reversed, with enhancement at the drain and suppression at the source. The line profiles of photocurrent along the channel (white dash line) at $V_{DS}$= ±0.5 and 0 V indicate the magnitudes of the induced and zero bias

photocurrents (Figure 3b). Similar observations on the SL FET are presented in Supporting Information S2. The photocurrent sign indicates that the applied electric field generates photocurrents that dominate contributions from the PTE effect and band bending at zero bias. The gate bias dependence of the photocurrents follows trends consistent with this interpretation. At large positive gate voltages, the Fermi level is shifted close to the conduction band, which decreases the built-in electric field near the $MoS_2$/Au interface (see Supporting Information S4). We observe a corresponding increase in the photocurrent magnitude. Depletion at negative gate voltages reduces band bending near the contacts, reducing the magnitude of the photocurrent. The decreasing channel resistance at increasing gate bias also contributes to an increase in photocurrent, as electrons must flow out the opposite contact to maintain charge neutrality .

In saturation (Figure 3c), positive photocurrent is observed throughout the device due to carrier drift generated by the large electric field. In further support of this interpretation, we identify the peak in the photocurrent at high drain-source biases (Figure 3d) with the space-charge region induced by pinch-off in the channel.[6,53] By integrating the photocurrent along the channel to generate an approximation of the local potential, one can observe that most of the applied voltage drops across the space-charge region, (dashed black line, $V_{DS}$=10 V).[56] We therefore conclude that the increase in photocurrent in the saturation regime mainly arises from more effective separation and collection of photoexcited carriers at high electric field. A recent study investigating the photocurrent in the saturation regime concludes that the generation current under global illumination is caused by the vanishing of pinch-off (in the space-charge region).[7] In the present study, the field distribution was probed directly, rather than inferred from the global photoresponse.

The dependencies of the photocurrent on gate bias and excitation power enable comparison of gate-induced and photogenerated carrier concentrations and transport mechanisms. The magnitude of the local photocurrent increases monotonically with gate voltage in a manner similar to the drain current (Figure 4a). The transition of the FET channel from accumulation to depletion is accompanied by a change in the power dependence of the photocurrent, reflecting the influence of the majority carrier concentration on photogenerated carrier recombination rates (Figure 4b). Specifically, the photocurrent becomes increasingly sub-linear as the transistor moves into depletion, reflecting the increasing rate of bimolecular recombination as the photogenerated carrier concentration exceeds the intrinsic carrier concentration. Simple estimates suggest (see Supporting Information S5) that the photogenerated carrier concentration is approximately $3x10^{11}$ $cm^{-2}$, whereas the intrinsic carrier concentration is ~$10^{10}$ $cm^{-2}$ at $V_g$=0 V.

A recent study of ohmically contacted SL-$MoS_2$ devices attributed photocurrent generated near the contacts to the PTE effect,[36] which arises from the difference in the Seebeck coefficients of the contact and channel materials in the presence of light-induced temperature gradients. At zero bias, both PTE and band-bending induced photocurrents are expected to produce photocurrents of opposite polarity at opposite contacts, as noted above. While the PTE must make some contribution to the photocurrent, the drain-source bias dependence of our data *cannot* be explained by a PTE effect. First, it is clear that the photocurrent signal in Figures 3c,d is controlled by the applied electric field. The minority carrier diffusion length (see Supporting information S3) is too small to enable direct collection of hot carriers at the contacts, so one can interpret the local photocurrent signal as probing the local electric field in the channel.[54] Second, the bias dependence of the photocurrent near the source and drain contacts in Figure 3a varies in the manner one would expect if the currents were dominated by electric field induced carrier

separation. There is likely to be a small contribution from PTE currents near the contacts, as has been observed for nanotubes[39] and graphene,[44,61] but these appear to be dominated by field effects in our devices under bias. In addition, the fast temporal response (~30 μs) observed in our devices (see Supporting information S6) rules out the PTE contribution resulting from heating of the contact junction, for which longer equilibration times are expected. Finally, the sub-linear dependence of the photocurrent (Figure 4b) rules out a PTE effect from electrons that have equilibrated with the lattice, as one would expect a linear power dependence in the signal.

In conclusion, spectrally and temporally resolved SPCM studies of $MoS_2$ FETs of varying channel thicknesses were carried out to identify the dominant photoresponse mechanisms. Photocurrents under bias are dominated by the field-assisted separation of photoexcited carriers as has been observed in graphene devices,[40,42,43] and the spectral dependence reveals the thickness-dependent transition from indirect to direct interband photoexcitation in $MoS_2$. Direct imaging of field-induced currents enables correlation of device saturation with channel pinch-off. The mechanistic understanding provided here will help guide the development of optoelectronic devices based on $MoS_2$. In addition, this further points to approaches for tailoring the photoresponse via chemical functionalization. Specifically, just as the gate voltage can modulate a photocurrent generated by drift/diffusion, the photoresponse can also be modulated by charge transfer to or from adsorbates/functional groups[62-64] or hybrid structures such as quantum dots similar to the case of graphene.[26,27,65,66]

## AUTHOR INFORMATION

### Corresponding Author

*Email: lauhon@northwestern.edu

## Notes

The authors declare no competing financial interest.

## ACKNOWLEDGEMENTS

This research was supported by the Materials Research Science and Engineering Center (MRSEC) of Northwestern University (NSF DMR-1121262). The authors thank B. Myers of NUANCE for assistance with electron beam lithography. This research made use of the NUANCE Center at Northwestern University, which is supported by NSF-NSEC, NSF-MRSEC, Keck Foundation, and the State of Illinois.

## ASSOCIATED CONTENT

### Supporting information

Experimental details, Raman spectroscopy, calculation of carrier lifetime and diffusion length, estimation of photoexcited and intrinsic carrier concentrations and time-resolved photoresponse. This material is free of charge via the Internet at http://pubs.acs.org.

### Figures:

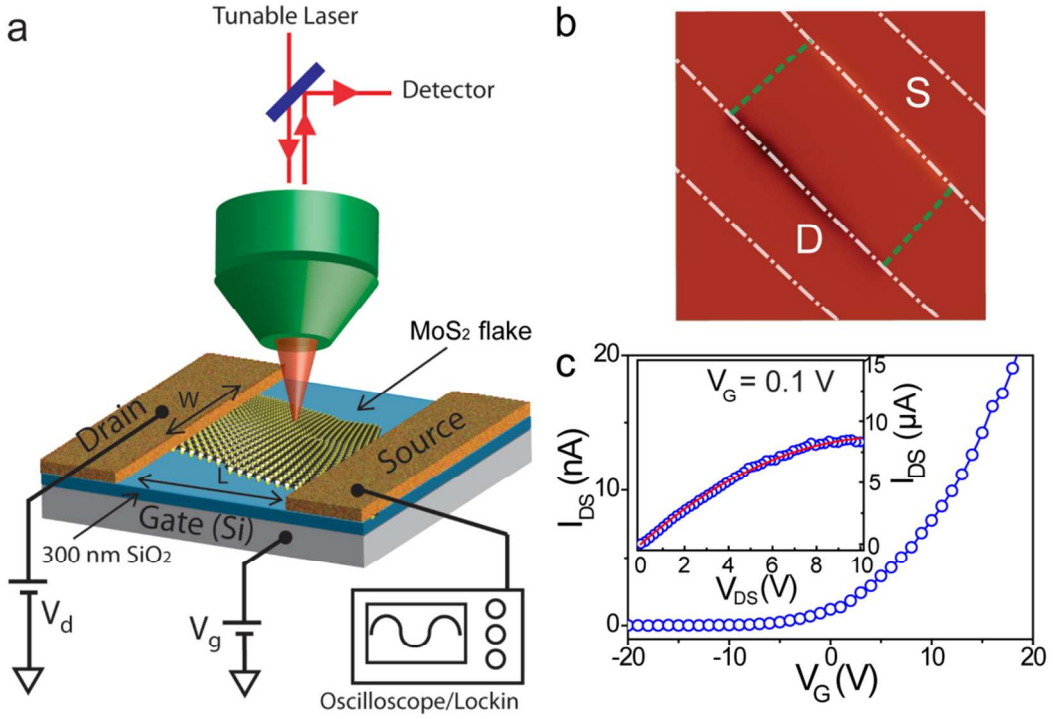


Figure 1. a) Schematic of the experimental setup for scanning photocurrent imaging of $MoS_2$ field-effect transistors (FETs). b) Scanning photocurrent image of a 4L $MoS_2$ FET acquired at $V_{DS}$, $V_G$ = 0 V, and λ= 550 nm. The white dashed lines indicate the position of source (S) and drain (D) contacts (1 μm width), and the green dashed lines indicate the perimeter of the 4L $MoS_2$ flake. c) Transfer curve of a 4L $MoS_2$ FET (L = 3.5 μm, W = 6.8 μm) at $V_{DS}$ = 10 mV. Inset: output curve at $V_G$=0.1 V.

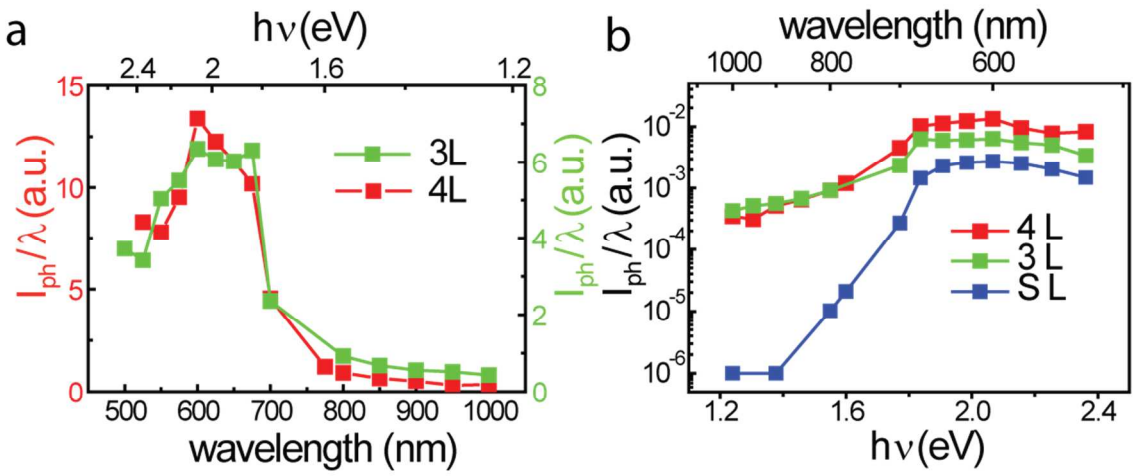


Figure 2. Photocurrent spectra at constant incident power (20 μW). To compensate for the difference in the incident photon flux, the measured photocurrents are normalized by the corresponding excitation wavelengths. a) Spectra of 3L and 4L $MoS_2$ on a linear scale. b) Comparison of SL, 3L, and 4L spectra on a semi-log scale.

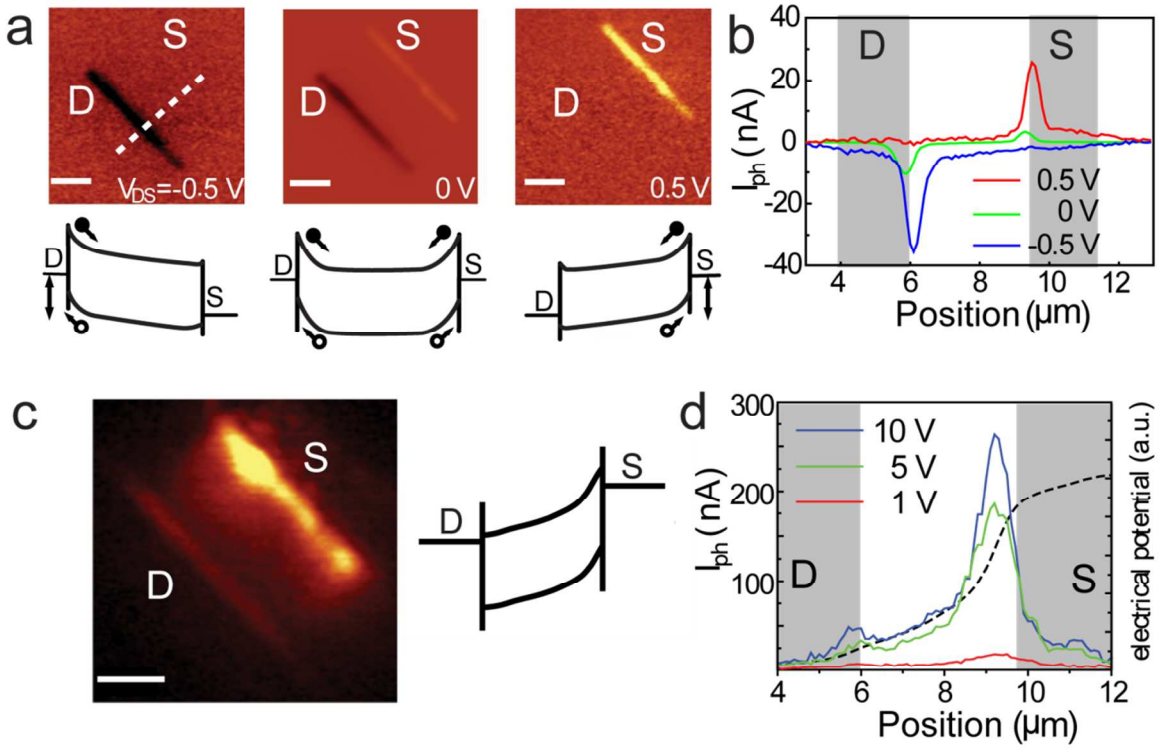


Figure 3. Drain-source bias dependence of photocurrents. a) Spatial photocurrent images in the linear region of a 4L FET at $V_{DS}$= 0.5, 0, and – 0.5 V, $V_G$=0 V shown along with the corresponding band diagrams ($V_G$ = 0 V). b) Corresponding line profiles of photocurrents along the channel (white dash line) at $V_{DS}$= 0.5, 0, and – 0.5 V c) (Left) Spatial photocurrent image recorded at $V_{DS}$=10 V and $V_G$=0.1 V (saturation regime). The channel length is 3.5 μm. (Right) Band diagram of $MoS_2$ FET in the saturation regime. d) Line profiles of photocurrents at different $V_{DS}$ and the approximate electrostatic potential along the channel (dashed black line, $V_{DS}$=10 V).

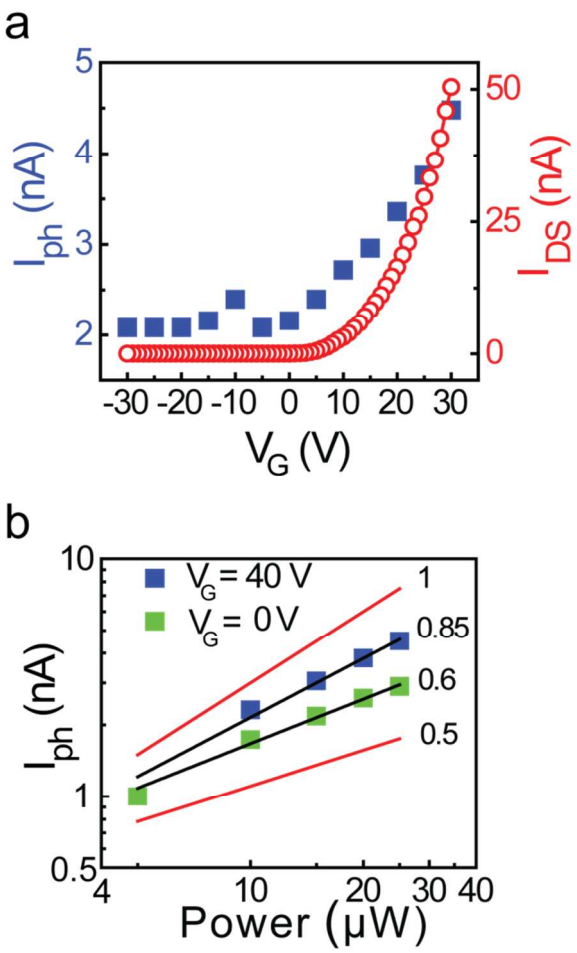


Figure 4. a) Photocurrent (blue) and drain current (red, $V_{DS}$=10 mV) as a function of $V_G$ for a 4L $MoS_2$ FET illuminated at $\lambda$=600 nm. b) Log-log plot of photocurrent amplitude as a function of excitation power ($\lambda$=600 nm) at $V_g$ = 40 V and 0 V. Linear and square root dependencies are shown as red lines for reference.

REFERENCES

(1) Wang, Q. H.; Kalantar-Zadeh, K.; Kis, A.; Coleman, J. N.; Strano, M. S. Electronics and optoelectronics of two-dimensional transition metal dichalcogenides. *Nat. Nanotech.* **2012**, *7*, 699-712.

(2) Mattheis, L. F. Energy Bands for 2H $NbSe_2$ and 2H-$MoS_2$. *Phys. Rev. Lett.* **1973**, *30*, 784-787.

(3) Mak, K. F.; He, K. L.; Shan, J.; Heinz, T. F. Control of valley polarization in monolayer $MoS_2$ by optical helicity. *Nat. Nanotech.* **2012**, *7*, 494-498.

(4) Mak, K. F. H., K.; Lee, C.; Lee, G. H.; Hone, J.; Heinz, T. F.; Shan, J. Tightly bound trions in monolayer $MoS_2$. *Nat. Mater.* **2012**, *12*, 207-211.

(5) Zeng, H. L.; Dai, J. F.; Yao, W.; Xiao, D.; Cui, X. D. Valley polarization in $MoS_2$ monolayers by optical pumping. *Nat. Nanotech.* **2012**, *7*, 490-493.

(6) Kim, S.; Konar, A.; Hwang, W. S.; Lee, J. H.; Lee, J.; Yang, J.; Jung, C.; Kim, H.; Yoo, J. B.; Choi, J. Y.; Jin, Y. W.; Lee, S. Y.; Jena, D.; Choi, W.; Kim, K. High-mobility and low-power thin-film transistors based on multilayer $MoS_2$ crystals. *Nat. Commun.* **2012**, *3*, 1011.

(7) Choi, W.; Cho, M. Y.; Konar, A.; Lee, J. H.; Cha, G.-B.; Hong, S. C.; Kim, S.; Kim, J.; Jena, D.; Joo, J.; Kim, S. High-Detectivity Multilayer $MoS_2$ Phototransistors with Spectral Response from Ultraviolet to Infrared. *Adv. Mater.* **2012**, *24*, 5832-5836.

(8) Wu, S.; Ross, J. S.; Liu, G.-B.; Aivazian, G.; Jones, A.; Fei, Z.; Zhu, W.; Xiao, D.; Yao, W.; Cobden, D.; Xu, X. Electrical tuning of valley magnetic moment through symmetry control in bilayer $MoS_2$. *Nat. Phys.* **2013**, *9*, 149-153.

(9) Radisavljevic, B.; Radenovic, A.; Brivio, J.; Giacometti, V.; Kis, A. Single-layer $MoS_2$ transistors. *Nat. Nanotech.* **2011**, *6*, 147-150.

(10) Lembke, D.; Kis, A. Breakdown of High-Performance Monolayer $MoS_2$ Transistors. *ACS Nano* **2012**, *6*, 10070-10075.

(11) Novoselov, K. S.; Jiang, D.; Schedin, F.; Booth, T. J.; Khotkevich, V. V.; Morozov, S. V.; Geim, A. K. Two-dimensional atomic crystals. *Proc. Nat. Acad. Sci. USA* **2005**, *102*, 10451-10453.

(12) Zhang, Y. J.; Ye, J. T.; Matsuhashi, Y.; Iwasa, Y. Ambipolar $MoS_2$ Thin Flake Transistors. *Nano Lett.* **2012**, *12*, 1136-1140.

(13) Jariwala, D.; Sangwan, V. K.; Late, D. J.; Johns, J. E.; Dravid, V. P.; Marks, T. J.; Lauhon, L. J.; Hersam, M. C. Band-like transport in high mobility unencapsulated single-layer $MoS_2$ transistors. *Applied Physics Letters* **2013**, *102*, 173107-173104.

(14) Grant, A. J.; Griffiths, T. M.; Pitt, G. D.; Yoffe, A. D. The electrical properties and the magnitude of the indirect gap in the semiconducting transition metal dichalcogenide layer crystals. *J. Phys. C.* **1975**, *8*, L17.

(15) Mak, K. F.; Lee, C.; Hone, J.; Shan, J.; Heinz, T. F. Atomically Thin $MoS_2$: A New Direct-Gap Semiconductor. *Phys. Rev. Lett.* **2010**, *105*, 136805.

(16) Splendiani, A.; Sun, L.; Zhang, Y. B.; Li, T. S.; Kim, J.; Chim, C. Y.; Galli, G.; Wang, F. Emerging Photoluminescence in Monolayer $MoS_2$. *Nano Lett.* **2010**, *10*, 1271-1275.

(17) Radisavljevic, B.; Whitwick, M. B.; Kis, A. Integrated Circuits and Logic Operations Based on Single-Layer $MoS_2$. *ACS Nano* **2011**, *5*, 9934-9938.

(18) Wang, H.; Yu, L.; Lee, Y.-H.; Shi, Y.; Hsu, A.; Chin, M. L.; Li, L.-J.; Dubey, M.; Kong, J.; Palacios, T. Integrated Circuits Based on Bilayer $MoS_2$ Transistors. *Nano Lett.* **2012**, *12*, 4674-4680.

(19) Yin, Z. Y.; Li, H.; Jiang, L.; Shi, Y. M.; Sun, Y. H.; Lu, G.; Zhang, Q.; Chen, X. D.; Zhang, H. Single-Layer $MoS_2$ Phototransistors. *ACS Nano* **2012**, *6*, 74-80.

(20) Lee, H. S.; Min, S. W.; Chang, Y. G.; Park, M. K.; Nam, T.; Kim, H.; Kim, J. H.; Ryu, S.; Im, S. $MoS_2$ Nanosheet Phototransistors with Thickness-Modulated Optical Energy Gap. *Nano Lett.* **2012**, *12*, 3695-3700.

(21) Duerloo, K.-A. N.; Ong, M. T.; Reed, E. J. Intrinsic Piezoelectricity in Two-Dimensional Materials. *The Journal of Physical Chemistry Letters* **2012**, *3*, 2871-2876.

(22) Komsa, H.-P.; Krasheninnikov, A. V. Two-Dimensional Transition Metal Dichalcogenide Alloys: Stability and Electronic Properties. *The Journal of Physical Chemistry Letters* **2012**, *3*, 3652-3656.

(23) Liu, Q.; Li, L.; Li, Y.; Gao, Z.; Chen, Z.; Lu, J. Tuning Electronic Structure of Bilayer $MoS_2$ by Vertical Electric Field: A First-Principles Investigation. *The Journal of Physical Chemistry C* **2012**, *116*, 21556-21562.

(24) Kou, L.; Tang, C.; Zhang, Y.; Heine, T.; Chen, C.; Frauenheim, T. Tuning Magnetism and Electronic Phase Transitions by Strain and Electric Field in Zigzag $MoS_2$ Nanoribbons. *The Journal of Physical Chemistry Letters* **2012**, *3*, 2934-2941.

(25) Ataca, C.; S□ahin, H.; Aktu□rk, E.; Ciraci, S. Mechanical and Electronic Properties of $MoS_2$ Nanoribbons and Their Defects. *The Journal of Physical Chemistry C* **2011**, *115*, 3934-3941.

(26) Kamat, P. V. Graphene-Based Nanoarchitectures. Anchoring Semiconductor and Metal Nanoparticles on a Two-Dimensional Carbon Support. *The Journal of Physical Chemistry Letters* **2009**, *1*, 520-527.

(27) Kamat, P. V. Graphene-Based Nanoassemblies for Energy Conversion. *The Journal of Physical Chemistry Letters* **2011**, *2*, 242-251.

(28) Kim, J.; Byun, S.; Smith, A. J.; Yu, J.; Huang, J. Enhanced Electrocatalytic Properties of Transition-Metal Dichalcogenides Sheets by Spontaneous Gold Nanoparticle Decoration. *The Journal of Physical Chemistry Letters* **2013**, *4*, 1227-1232.

(29) Zong, X.; Wu, G.; Yan, H.; Ma, G.; Shi, J.; Wen, F.; Wang, L.; Li, C. Photocatalytic $H_2$ Evolution on $MoS_2$/CdS Catalysts under Visible Light Irradiation. *The Journal of Physical Chemistry C* **2010**, *114*, 1963-1968.

(30) Frame, F. A.; Osterloh, F. E. CdSe-$MoS_2$: A Quantum Size-Confined Photocatalyst for Hydrogen Evolution from Water under Visible Light. *The Journal of Physical Chemistry C* **2010**, *114*, 10628-10633.

(31) Min, S.; Lu, G. Sites for High Efficient Photocatalytic Hydrogen Evolution on a Limited-Layered $MoS_2$ Cocatalyst Confined on Graphene Sheets—The Role of Graphene. *The Journal of Physical Chemistry C* **2012**, *116*, 25415-25424.

(32) Liu, Y.; Yu, Y.-X.; Zhang, W.-D. $MoS_2$/CdS Heterojunction with High Photoelectrochemical Activity for $H_2$ Evolution under Visible Light: The Role of $MoS_2$. *The Journal of Physical Chemistry C* **2013**, *117*, 12949-12957.

(33) Kamat, P. V. Manipulation of Charge Transfer Across Semiconductor Interface. A Criterion That Cannot Be Ignored in Photocatalyst Design. *The Journal of Physical Chemistry Letters* **2012**, *3*, 663-672.

(34) Chen, Z.; Forman, A. J.; Jaramillo, T. F. Bridging the Gap Between Bulk and Nanostructured Photoelectrodes: The Impact of Surface States on the Electrocatalytic and Photoelectrochemical Properties of $MoS_2$. *The Journal of Physical Chemistry C* **2013**, *117*, 9713-9722.

(35) Fontana, M.; Deppe, T.; Boyd, A. K.; Rinzan, M.; Liu, A. Y.; Paranjape, M.; Barbara, P. Electron-hole transport and photovoltaic effect in gated $MoS_2$ Schottky junctions. *Scientific Reports* **2013**, *3*.

(36) Buscema, M. B., M.; Zwiller, M.; van der Zant, H. S. J.; Steele, G. A.; Castellanos-Gomez, A. . Large and Tunable Photothermoelectric Effect in Single-Layer $MoS_2$. *Nano Lett.* **2013**, *13*, 358-363.

(37) St-Antoine, B. C.; Menard, D.; Martel, R. Position Sensitive Photothermoelectric Effect in Suspended Single-Walled Carbon Nanotube Films. *Nano Lett.* **2009**, *9*, 3503-3508.

(38) St-Antoine, B. C.; Menard, D.; Martel, R. Photothermoelectric effects in single-walled carbon nanotube films: Reinterpreting scanning photocurrent experiments. *Nano Res.* **2012**, *5*, 73-81.

(39) Sczygelski, E.; Sangwan, V. K.; Wu, C.-C.; Arnold, H. N.; Everaerts, K.; Marks, T. J.; Hersam, M. C.; Lauhon, L. J. Extrinsic and intrinsic photoresponse in monodisperse carbon nanotube thin film transistors. *Appl. Phys. Lett.* **2013**, *102*, 083104-083105.

(40) Freitag, M.; Low, T.; Xia, F.; Avouris, P. Photoconductivity of biased graphene. *Nat. Photon.* **2013**, *7*, 53-59.

(41) Freitag, M.; Low, T.; Avouris, P. Increased Responsivity of Suspended Graphene Photodetectors. *Nano Letters* **2013**, *13*, 1644-1648.

(42) Mueller, T.; Xia, F.; Freitag, M.; Tsang, J.; Avouris, P. Role of contacts in graphene transistors: A scanning photocurrent study. *Physical Review B* **2009**, *79*, 245430.

(43) Xia, F.; Mueller, T.; Golizadeh-Mojarad, R.; Freitag, M.; Lin, Y.-m.; Tsang, J.; Perebeinos, V.; Avouris, P. Photocurrent Imaging and Efficient Photon Detection in a Graphene Transistor. *Nano Letters* **2009**, *9*, 1039-1044.

(44) Peters, E. C.; Lee, E. J.; Burghard, M.; Kern, K. Gate dependent photocurrents at a graphene pn junction. *Applied Physics Letters* **2010**, *97*, 193102-193102-193103.

(45) Lee, E. J. H.; Balasubramanian, K.; Weitz, R. T.; Burghard, M.; Kern, K. Contact and edge effects in graphene devices. *Nat. Nanotech.* **2008**, *3*, 486-490.

(46) Gabor, N. M.; Song, J. C.; Ma, Q.; Nair, N. L.; Taychatanapat, T.; Watanabe, K.; Taniguchi, T.; Levitov, L. S.; Jarillo-Herrero, P. Hot carrier–assisted intrinsic photoresponse in graphene. *Science* **2011**, *334*, 648-652.

(47) Sun, D.; Aivazian, G.; Jones, A. M.; Ross, J. S.; Yao, W.; Cobden, D.; Xu, X. Ultrafast hot-carrier-dominated photocurrent in graphene. *Nature Nanotechnology* **2012**, *7*, 114-118.

(48) Graham, M. W.; Shi, S.-F.; Ralph, D. C.; Park, J.; McEuen, P. L. Photocurrent measurements of supercollision cooling in graphene. *Nat Phys* **2013**, *9*, 103-108.

(49) Lee, C.; Yan, H.; Brus, L. E.; Heinz, T. F.; Hone, J.; Ryu, S. Anomalous Lattice Vibrations of Single- and Few-Layer $MoS_2$. *ACS Nano* **2010**, *4*, 2695-2700.

(50) Ayari, A.; Cobas, E.; Ogundadegbe, O.; Fuhrer, M. S. Realization and electrical characterization of ultrathin crystals of layered transition-metal dichalcogenides. *J. Appl. Phys.* **2007**, *101*, 014507.

(51) Li, H.; Yin, Z. Y.; He, Q. Y.; Huang, X.; Lu, G.; Fam, D. W. H.; Tok, A. I. Y.; Zhang, Q.; Zhang, H. Fabrication of Single- and Multilayer $MoS_2$ Film-Based Field-Effect Transistors for Sensing NO at Room Temperature. *Small* **2012**, *8*, 63-67.

(52) Liu, H.; Neal, A. T.; Ye, P. D. D. Channel Length Scaling of $MoS_2$ MOSFETs. *ACS Nano* **2012**, *6*, 8563-8569.

(53) Sze, S. M. *Physics of Semiconductor devices 2nd Edition*; John Wiley & Sons, 2002.

(54) Allen, J. E.; Perea, D. E.; Hemesath, E. R.; Lauhon, L. J. Nonuniform Nanowire Doping Profiles Revealed by Quantitative Scanning Photocurrent Microscopy. *Adv. Mater.* **2009**, *21*, 3067-3072.

(55) Sundaram, R. S. E., M.; Lombardo, A.; Krupke, R.; Ferrari, A.C.; Avouris, PH.; Steiner. M. Electroluminescence in Single Layer $MoS_2$. *Nano Lett.* **2013**, *13*, 1416-1421.

(56) Allen, J. E.; Hemesath, E. R.; Lauhon, L. J. Scanning Photocurrent Microscopy Analysis of Si Nanowire Field-Effect Transistors Fabricated by Surface Etching of the Channel. *Nano Lett.* **2009**, *9*, 1903-1908.

(57) Ahn, Y.; Dunning, J.; Park, J. Scanning photocurrent imaging and electronic band studies in silicon nanowire field effect transistors. *Nano Lett.* **2005**, *5*, 1367-1370.

(58) Hyun, J. K.; Lauhon, L. J. Spatially Resolved Plasmonically Enhanced Photocurrent from Au Nanoparticles on a Si Nanowire. *Nano Lett.* **2011**, *11*, 2731-2734.

(59) Freitag, M.; Tsang, J. C.; Bol, A.; Yuan, D. N.; Liu, J.; Avouris, P. Imaging of the schottky barriers and charge depletion in carbon nanotube transistors. *Nano Lett.* **2007**, *7*, 2037-2042.

(60) Lee, E. J. H.; Balasubramanian, K.; Dorfmuller, J.; Vogelgesang, R.; Fu, N.; Mews, A.; Burghard, M.; Kern, K. Electronic-band-structure mapping of nanotube transistors by scanning photocurrent microscopy. *Small* **2007**, *3*, 2038-2042.

(61) Park, J.; Ahn, Y. H.; Ruiz-Vargas, C. Imaging of Photocurrent Generation and Collection in Single-Layer Graphene. *Nano Lett.* **2009**, *9*, 1742-1746.

(62) Li, Y.; Wu, D.; Zhou, Z.; Cabrera, C. R.; Chen, Z. Enhanced Li Adsorption and Diffusion on $MoS_2$ Zigzag Nanoribbons by Edge Effects: A Computational Study. *The Journal of Physical Chemistry Letters* **2012**, *3*, 2221-2227.

(63) Ataca, C.; Ciraci, S. Functionalization of Single-Layer $MoS_2$ Honeycomb Structures. *The Journal of Physical Chemistry C* **2011**, *115*, 13303-13311.

(64) Andersen, A.; Kathmann, S. M.; Lilga, M. A.; Albrecht, K. O.; Hallen, R. T.; Mei, D. Adsorption of Potassium on $MoS_2$(100) Surface: A First-Principles Investigation. *The Journal of Physical Chemistry C* **2011**, *115*, 9025-9040.

(65) Li, X. D.; Yu, S.; Wu, S. Q.; Wen, Y. H.; Zhou, S.; Zhu, Z. Z. Structural and Electronic Properties of Superlattice Composed of Graphene and Monolayer $MoS_2$. *The Journal of Physical Chemistry C* **2013**, *10.1021/jp404080z*.

(66) Radich, J. G.; Dwyer, R.; Kamat, P. V. $Cu_2S$ Reduced Graphene Oxide Composite for High-Efficiency Quantum Dot Solar Cells. Overcoming the Redox Limitations of $S_2$–/$Sn_2$– at the Counter Electrode. *The Journal of Physical Chemistry Letters* **2011**, *2*, 2453-2460.

TABLE OF CONTENTS FIGURE

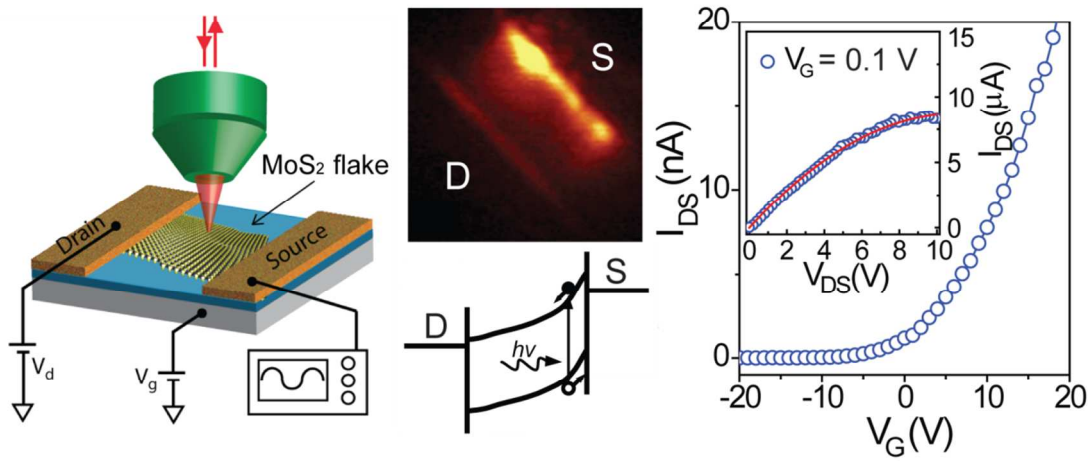


KEYWORDS: $MoS_2$, transition metal dichalcogenides, scanning photocurrent microscopy, nanoelectronics.